

Tilted and type-III Dirac cones emerging from flat bands in photonic orbital graphene

M. Milicevic¹, G. Montambaux², T. Ozawa³, I. Sagnes¹, A. Lemaître¹, L. Le Gratiet¹, A. Harouri¹, J. Bloch¹, A. Amo^{4*}

¹Centre de Nanosciences et de Nanotechnologies, CNRS, Univ. Paris-Sud, Université Paris-Saclay, C2N-Marcoussis, 91460 Marcoussis, France

²Laboratoire de Physique des Solides, CNRS, Univ. Paris-Sud, Université Paris-Saclay, 91405 Orsay Cedex, France

³ Interdisciplinary Theoretical and Mathematical Sciences Program (iTHEMS), RIKEN, Wako, Saitama 351-0198, Japan

⁴Univ. Lille, CNRS, UMR 8523 – PhLAM – Physique des Lasers Atomes et Molécules, F-59000 Lille, France

*alberto.amo-garcia@univ-lille.fr

The extraordinary electronic properties of Dirac materials, the two-dimensional partners of Weyl semimetals, arise from the linear crossings in their band structure. When the dispersion around the Dirac points is tilted, the emergence of intricate transport phenomena has been predicted, such as modified Klein tunnelling, intrinsic anomalous Hall effects and ferrimagnetism. However, Dirac materials are rare, particularly with tilted Dirac cones. Recently, artificial materials whose building blocks present orbital degrees of freedom have appeared as promising candidates for the engineering of exotic Dirac dispersions. Here we take advantage of the orbital structure of photonic resonators arranged in a honeycomb lattice to implement photonic lattices with semi-Dirac, tilted and, most interestingly, type-III Dirac cones that combine flat and linear dispersions. The tilted cones emerge from the touching of a flat and a parabolic band with a non-trivial topological charge. These results open the way to the synthesis of orbital Dirac matter with unconventional transport properties and, in combination with polariton nonlinearities, to the study of topological and Dirac superfluids in photonic lattices.

The extraordinary transport properties of Dirac materials arise from the spinor nature of their electronic wavefunctions and from the linear dispersion around Dirac and Weyl points. In two-dimensions, Klein tunnelling, weak antilocalisation, unconventional Landau levels or bulk pseudo-confinement appear as some of their most remarkable features^{1,2}. Standard Dirac cones, like those present in graphene and other two-dimensional materials, have rotational symmetry about the Dirac quasi-momentum. Their topological properties make them particularly robust to deformations of the lattice: Dirac cones always appear in pairs, each of them characterised by a topological charge³, and in the presence of time-reversal and inversion symmetry, they can only be annihilated via their merging with a Dirac point of opposite charge⁴⁻⁹.

Dirac cones can be classified according to the geometry of their Fermi surface. The cylindrically symmetric Dirac cones described above belong to the family of type-I Dirac cones. They are characterised by a closed Fermi surface eventually becoming a single point at the band crossing, where the density of states vanishes (Fig. 1a). However, they are not the only kind of linear band crossings that can be found in Dirac materials. The general Hamiltonian describing a Dirac cone in two dimensions can be expressed as¹⁰ $H(\mathbf{q}) = (v_{0x}q_x + v_{0y}q_y)\sigma_0 + v_xq_x\sigma_a + v_yq_y\sigma_b$, where $q_{x,y}$ is the wave vector measured from the Dirac point; v_{0x} , v_{0y} , v_x and v_y represent effective velocities; σ_0 is the 2×2 identity matrix and $\sigma_{a,b} = \mathbf{u}_{a,b} \cdot \boldsymbol{\sigma}$, where $\mathbf{u}_{a,b}$ are suitably chosen orthogonal unit vectors and $\boldsymbol{\sigma} = (\sigma_x, \sigma_y, \sigma_z)$ is the vector of Pauli matrices. The eigenenergies of this Hamiltonian form two bands:

$$E_{\pm}(\mathbf{k}) = v_{0x}q_x + v_{0y}q_y \pm \sqrt{(v_xq_x)^2 + (v_yq_y)^2}. \quad (1)$$

If both coefficients v_{0x} and v_{0y} are equal to zero we obtain the energy spectrum of a type-I Dirac cone with Fermi velocities v_x and v_y . If any of the v_{0x}, v_{0y} coefficients is non zero, then the Dirac cone is tilted (Fig. 1(b)). In two dimensional materials, this kind of tilted Dirac dispersion has been predicted to appear in quinooid-type¹⁰ and hydrogenated graphene¹¹, and it has been indirectly evidenced in the organic semiconductor^{10,12,13} α -(BEDT-TTF)₂I₃. The interest of materials presenting this dispersion

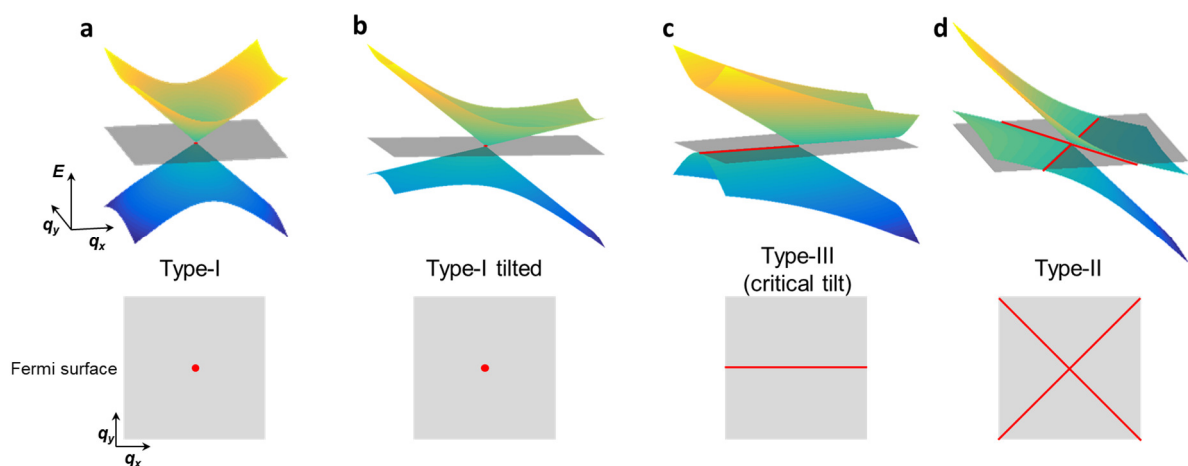


Figure 1. Types of Dirac dispersions in two dimensions. (top) Dispersions together with the zero energy plane (grey); (bottom, in red) zero-energy Fermi surface: **a** Standard, type-I Dirac cones characterised by a linear dispersion in all directions in k -space and a point-like Fermi surface. **b** Type-I tilted Dirac cone. **c** Type-III Dirac point (critically tilted), combining a flat band along a line and linear dispersions. Its Fermi surface is a line. **d** Type-II Dirac cone.

resides in its non-isotropic transport properties, which can be used for valley filtering in p–n junctions¹⁴ or for the generation of photocurrent¹⁵.

When the tilt parameter $\tilde{v}_0 \equiv \sqrt{(v_{0x}/v_x)^2 + (v_{0y}/v_y)^2}$ is larger than 1, a type-II Dirac point^{10,16} is formed (Fig. 1d). Its Fermi surface is no longer a point but two crossing lines, and the density of states at the energy of the Dirac point becomes finite¹⁶. They have been recently observed in the form of Fermi arcs in three-dimensional semimetals^{17–19}. A particularly interesting situation takes place at the transition between type-I and type-II Dirac cones, that is, when the tilt parameter $\tilde{v}_0 = 1$. In this case, the cone is critically tilted, with a flat band along one direction (Fig. 1c). Because of its distinct Fermi surface, a single line, and its diverging density of states, this kind of dispersion has been labelled type-III Dirac cone^{20,21}. While most of their electric and magnetic properties are still to be unveiled, they have been predicted to greatly enhance the superconducting gap in Weyl semimetals²², and provide a new platform for the study of correlated phases with a flat band²³.

Type-III Dirac points have not been yet reported experimentally, and tilted type-I and type-II have been challenging to synthesize^{13,17,19} because they require materials whose constituent atoms are arranged in lattices with intricate electron hoppings^{10,12,16}. Existing proposals rely on the engineering of next-nearest neighbours tunnelling, difficult to find in natural materials and to implement in electronic metamaterials. Artificial photonic lattices represent an opportunity to explore the physics of unconventional Dirac points thanks to the at-will control of onsite energies and hoppings²⁴. Current schemes are based on the design of long distant coupling of photons in lattices of resonators^{25,26}; evidence of type-II Weyl points has been recently reported in microwave metamaterials^{27,28} and via conical diffraction in laser written waveguides with elaborate couplings²⁹.

In this article we propose and demonstrate experimentally a new method to implement tilted and semi-Dirac cones for photons, and provide the first experimental observation of type-III Dirac cones. We employ p_x, p_y orbital bands in a honeycomb lattice of polariton micropillars, which arise from the nearest-neighbour hopping of photons confined in the first excited modes of each resonator of the lattice^{30,31}. In this analogue system, the band structure is directly accessible in photoluminescence experiments. The orbital bands with symmetric hoppings contain a flat band that touches a parabolic band. When asymmetry in the hopping is introduced, which simulates uniaxial strain in solid-state graphene, the flat-parabolic band touching evolves into tilted and type-III Dirac cones. The richness of this multi-band system allows, in addition, the observation of semi-Dirac cones which combine massless and massive dispersions. By analysing their topological charge, i.e. the winding of the Hamiltonian around each Dirac point, we show that the semi-Dirac, tilted and type-III Dirac cones emerge as a consequence of topological Lifshitz transitions induced by strain in the orbital bands. The present realisation shows the potential of orbital bands to engineer the properties of Dirac matter.

Photonic orbital lattice

The photonic platform we employ is a honeycomb lattice of coupled micropillars. The lattice is etched from a semiconductor planar microcavity made out of two AlGaAs Bragg mirrors that confine photons in the vertical direction, and twelve GaAs quantum wells embedded in the spacer between the mirrors (see Sec. I of Supplementary Information). At 10 K, the temperature of our experiments, the confined photons and the quantum well excitons are in the strong coupling regime and form polaritons, light-matter hybrid quasi-particles. Each micropillar, with a diameter of 2.75 μm presents an additional

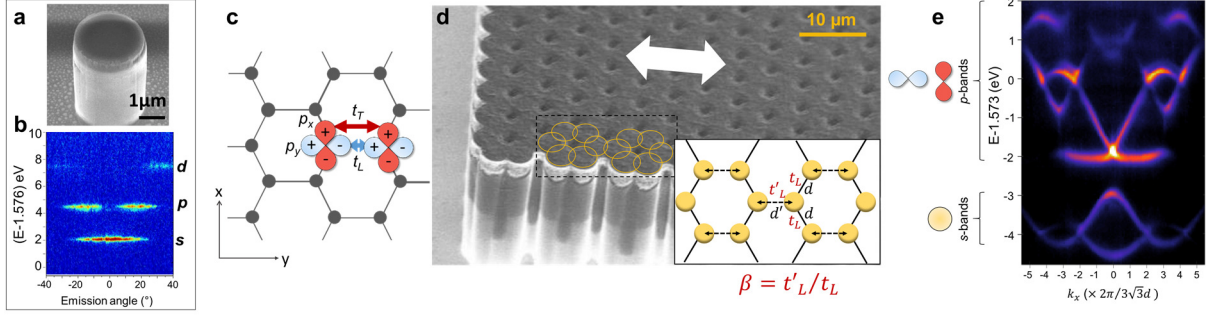


Figure 2. Honeycomb polariton lattice with orbital bands. Scanning electron microscopy (SEM) image of a single micropillar, the elementary building block of the honeycomb lattice. **b** Characteristic emission spectrum of a single micropillar, showing s, p and d discrete modes. **c** Scheme of the coupling of p_x and p_y orbitals in the honeycomb lattice with hoppings $t_L \gg t_T$. **d** Image of a honeycomb lattice of micropillars with homogeneous hoppings ($t_L = t'_L$, $\beta = 1$, see inset). The circles pinpoint the upper surface of the micropillars in two adjacent hexagons; the white arrows indicate the direction along which the coupling t'_L is modified. **e** Experimental photoluminescence of the lattice showing s- and p-bands.

lateral confinement due to the index of refraction contrast between the semiconductor and air (Fig. 2a). The photonic spectrum of an individual micropillar is thus discrete with the lowest energy s-mode being cylindrically symmetric, and the first excited modes formed by two degenerate p_x, p_y orbitals with lobes oriented 90° from each other (Fig. 2b)³¹. In the honeycomb lattice, the micropillars overlap (centre-to-centre distance $d = 2.4 \mu\text{m}$) enabling the hopping of photons between adjacent sites (Fig. 2d).

The coupling of s-modes results in two bands with a spectrum and eigenmodes very similar to those of electrons in graphene, shown in the low energy part of Fig. 2e and studied in previous works^{30,32}. Here we concentrate on the orbital bands which arise from the coupling of p-modes (high-energy set of bands in Fig. 2e). Orbitals oriented along the link between adjacent pillars (p_y in the example of Fig. 2c) present a coupling t_L much stronger than t_T , the coupling of orbitals oriented perpendicular to the link (p_x in Fig. 2c).

Figure 3a shows the angle resolved photoluminescence of the p-bands when exciting the lattice at its centre with a non-resonant continuous wave laser at 745 nm, focused on a $3 \mu\text{m}$ diameter spot. The power of the laser is 6 mW, well below the threshold for any nonlinear effect. The laser creates electrons and holes in the quantum wells that relax down through phonon scattering to form polaritons distributed over the different bands of the lattice. When polaritons recombine via the escape of a photon out of the microcavity, photons are emitted with an in-plane momentum and a frequency that correspond to those of the original polaritons within the lattice of resonators. An angle and energy resolved measurement employing an imaging spectrometer coupled to a CCD allows reconstructing the dispersion relation (see Supplementary Information). To avoid destructive interference effects along high symmetric crystallographic directions, characteristic of bi-partite lattices³³, we record the emission as a function of k_x for $k_y = 4\pi/3d$, passing through the K, Γ, K' points in the second Brillouin zone (dashed line in Fig. 3e). Four bands are observed: the lowest one is flat, while the two central bands present two type-I Dirac points at K and K' and touch the flat band at the Γ point³⁰. This is in good agreement with a nearest-neighbour tight-binding calculation³⁴ assuming $t_T = 0$ (white solid lines, see Supplementary Information). In the experiments, the uppermost band

deviates from a flat band due to the coupling to higher energy bands (arising from photonic d-orbitals in the micropillars).

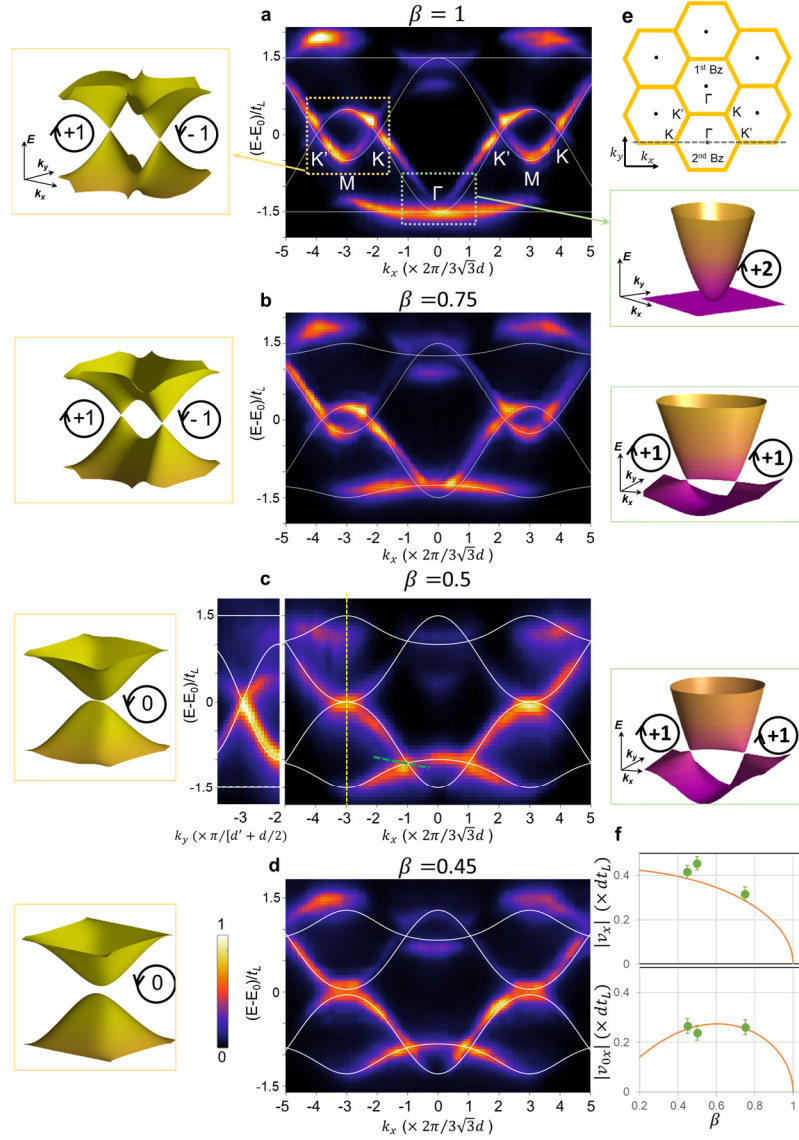


Figure 3. Tilted Dirac cones in orbital graphene under strain. The central panels **a-d** show the measured polariton photoluminescence intensity as a function of k_x for different values of β (the colour scale of each panel has been independently normalised to its maximum value). The cut is done for $k_y = 2\pi/(d' + d/2)$, dashed line in **e**. $d = 2.40 \mu\text{m}$ for the unstrained coupling, while for the strained coupling d' is $2.40 \mu\text{m}$, $2.60 \mu\text{m}$, $2.70 \mu\text{m}$ and $2.72 \mu\text{m}$, respectively, in **a-d**. $E_0 = 1.5687 \text{ eV}$ and photon-exciton detuning $\delta = -10 \text{ meV}$ at the energy minimum of the p-bands for panels **a, b, d**; $E_0 = 1.5780 \text{ meV}$ and $\delta = -2 \text{ meV}$ for **c**. $\hbar t_L = -0.90 \text{ meV}$ for panel **a**, -0.85 meV for **b** and **d**, and -0.65 for **c**, which are obtained by fitting the measured spectra with a tight-binding Hamiltonian (fits are shown in white lines). The left inset of **c** shows the semi-Dirac dispersion measured along k_y for the value of k_x marked by a dashed line in **c**. The left column, depicts the calculated tight-binding bands for energies close to E_0 (orange dashed rectangle in **a**) and the winding of the wavefunctions around the Dirac points. The right column shows the tight-binding bands in the region at the bottom of the bands (green dashed rectangle in **a**) together with the winding of the wavefunctions. **e** Sketch of the Brillouin zones in momentum space. **f** Green dots: absolute value of v_x and v_{0x} extracted from fits of Eq. 1 to the two experimental Dirac cones visible at low energies in **b-d** (see Supplementary Information). The plotted value is the average of $|v_x|$ and $|v_{0x}|$ extracted from the two Dirac points. Solid lines: tight-binding result.

Tilted and semi-Dirac cones

The dispersion of the p-bands can be modified by introducing an artificial uniaxial strain in the lattice. To do so, we change the centre-to-centre distance d' between the micropillars whose link is oriented along the y direction. This is equivalent to modifying t'_L , defined in the inset of Fig. 2d, while keeping the other two couplings t_L constant³⁵. The central panels of Fig. 3 show the spectra of four different lattices with decreasing strain parameters $\beta \equiv t'_L/t_L$. The value of β is extracted from the fit of the tight-binding model (white lines) to the experimental dispersions. Let us first focus on the type-I Dirac cones in the central region (orange rectangle). The left panels depict the calculated dispersion around E_0 obtained from the tight-binding model. Decreasing beta, that is, emulating the stretching of the lattice, brings the Dirac cones closer together in the x direction (Fig. 3a-b) until they merge at $\beta = 0.5$ in a single band touching (Fig. 3c). For $\beta < 0.5$ a gap is opened (Fig. 3d and Supplementary Fig. S4). This is a topological Lifshitz transition in which two Dirac cones with opposite topological charge merge and annihilate, predicted for standard s-band graphene^{4,36} and reported in photonic^{7,8} and atomic^{5,6} honeycomb lattices and in black phosphorus⁹. At the merging point ($\beta = 0.5$, Fig. 3c), we provide the direct observation of a semi-Dirac dispersion, with the touching of two parabolic bands along the k_x direction and a linear dispersion along k_y (shown in the left inset of Fig. 3c).

The Dirac points that we have just analysed do not present any tilt: $v_{0x} = v_{0y} = 0$ for any value of the strain. Tilted Dirac cones become apparent when analysing the evolution of the touching between the quadratic and flat bands (green dashed square in Fig. 3a) as a function of strain. For decreasing values of β , the flat band evolves into a dispersive band with negative effective mass at the Γ point, and the band touching divides into two Dirac points that move away from each other in the k_x direction³⁷ (Fig. 3b-e). Remarkably, they are tilted as indicated by the angle bisector in green dashed lines in Fig. 3c. A fit of Eq. 1 to the experimental dispersions close to the Dirac points reveals the evolution of v_{0x} and v_x as a function of the strain, as depicted in Fig. 3f. The measured values of the tilt (v_{0x}) agree well with those expected from the tight-binding Hamiltonian shown as solid lines in Fig. 3f (see Supplementary Information).

Engineering type-III Dirac cones

Critically tilted type-III Dirac cones with $\tilde{v}_0 = \sqrt{(v_{0x}/v_x)^2 + (v_{0y}/v_y)^2} = 1$ can be engineered in our system when instead of expanding the lattice ($\beta < 1$), it is compressed ($\beta > 1$). This is shown in Fig. 4 for $\beta = 1.5$: in the direction k_y (Fig. 4c), parallel to that along which d' is reduced, two new Dirac points emerge from the flat-parabolic band touching. As a reference, Fig. 4a shows the case of $\beta = 1$ along k_y . The most striking feature of the new Dirac points is that they show the crossing of a flat band with zero group velocity and a linear band with finite group velocity (see Fig. 4c, dashed rectangle). This is precisely the signature of a type-III Dirac cone, and it implies $v_{0y} = -v_y$. From the experimental photoluminescence of Fig 4c we measure $|v_{0y}| = (0.29 \pm 0.03)\bar{d}t_L$ and $|v_y| = (0.35 \pm 0.03)\bar{d}t_L$ (with $\bar{d} = \frac{2d'+d}{3}$), which is in good agreement with the tight binding prediction ($|v_{0y}| = |v_y| = 0.37dt_L$, see Supplementary Information). Along the perpendicular direction (k_x , Fig. 4d), the type-III cones present a symmetric linear crossing, and we measure $|v_{0x}| = (0.00 \pm 0.04)dt_L$, $|v_x| = (0.46 \pm 0.04)dt_L$, in agreement with the tight-binding Hamiltonian (0 and $0.48dt_L$, respectively), whose dispersion is shown in Fig. 4e. The degeneracy of the flat band results in a divergent density of states at the energy of the type-III Dirac point.

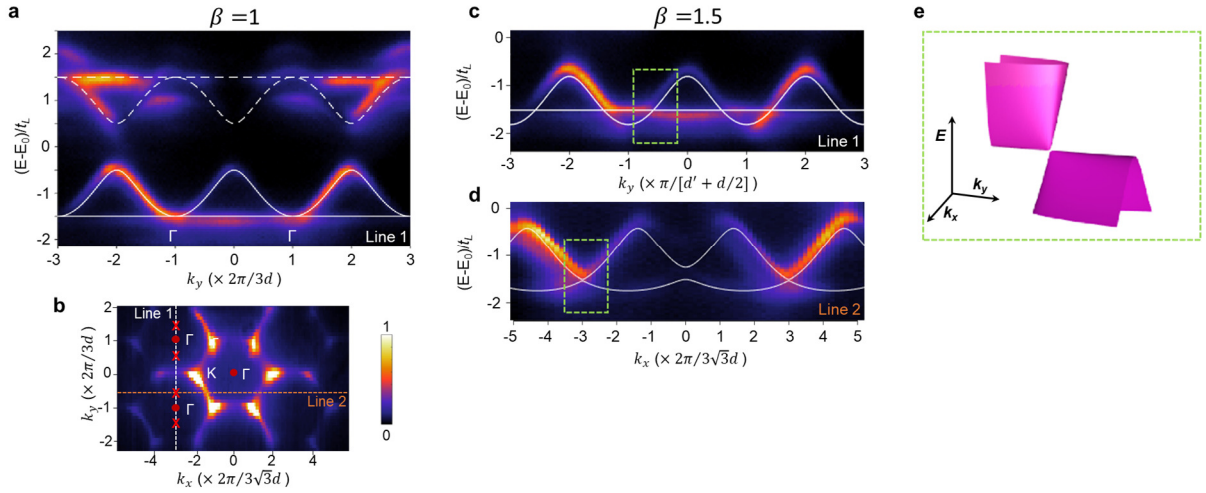


Figure 4. Type-III Dirac cones. **a** Measured photoluminescence intensity for $\beta = 1$ ($d = d' = 2.60 \mu\text{m}$) along k_y for $k_x = -2\pi/\sqrt{3}d$ (line 1 in **b**). $E_0 = 1.5687 \text{ eV}$ and $\hbar t_L = -0.85 \text{ meV}$. **b** Emission in momentum space at E_0 for $\beta = 1$, showing the usual Dirac points at the high symmetry points in reciprocal space. Crosses indicate the position of the Dirac points reported in **c**. **c** Zoom of the low energy section of the measured spectrum for a lattice with $\beta = 1.5$ ($d = 2.60 \mu\text{m}$, $d' = 2.40 \mu\text{m}$) showing the emergence of a type-III Dirac cone combining flat and dispersive bands. **d** Measured dispersion along the k_x direction for $k_y = -0.5 \times 2\pi/3d$ (line 2 in **b**), crossing the Dirac point in the dashed rectangle in **c**. **e** Dispersion obtained from the tight-binding model zoomed in the momentum space region marked with a dashed rectangle in **c** and **d**. In **a**, **c**, **d**, the white lines show the tight-binding model.

Topological invariants of tilted and type-III Dirac cones

The emergence of unconventional Dirac cones when applying a uniaxial deformation to the orbital lattice can be understood from topological arguments. The analysis of the topological charge associated to each cone, that is, the winding of the Hamiltonian around each Dirac point, provides a clear picture of their birth and evolution. The vicinity of the band touching point around the Γ point for $\beta = 1$ can be described by an effective 2×2 Hamiltonian obtained from the projection of the full 4×4 Hamiltonian on the subspace of the two lowest energy bands³⁸, resulting in the following effective Hamiltonian:

$$H(\mathbf{q}) = -\frac{3}{2}t_L\sigma_0 + \frac{3}{8}t_L \begin{pmatrix} q_x^2 & q_x q_y \\ q_x q_y & q_y^2 \end{pmatrix} \equiv -\frac{3}{2}t_L\sigma_0 + \mathbf{h}(\mathbf{q}) \cdot \boldsymbol{\sigma}. \quad (2)$$

Matrix elements coupling the high and low energy manifolds are treated in a second order perturbation theory³⁸. In this form, the winding of $\mathbf{h}(\mathbf{q})$ can be calculated as a winding vector³⁶: $\mathcal{W} = (2\pi)^{-1} \oint \mathbf{n}(\mathbf{q}) \times d\mathbf{n}(\mathbf{q})$, where $\mathbf{n}(\mathbf{q}) = \frac{\mathbf{h}(\mathbf{q})}{|\mathbf{h}(\mathbf{q})|}$, and the integral is performed along a closed line in momentum space that encircles the band touching point (see Supplementary Information). The modulus of \mathcal{W} is always an integer, thus providing a topological charge to the touching point, and it has a value $\mathcal{W} = 2$ in this case.

We can extend this analysis to the emerging Dirac cones when $\beta \neq 1$. Following the same procedure, the tight-binding Hamiltonian can be reduced to an effective 2×2 matrix close to the considered Dirac cone. For $\beta < 1$, the energy of the Dirac cones in the lower part of the spectrum is $E_D = E_0 - \frac{1}{2}\sqrt{3 + 6\beta^2}t_L$. Taking E_D as the origin of energies, the effective Hamiltonian near a Dirac point reads:

$$H(\mathbf{q}) = v \cos \theta q_x \sigma_0 + v q_x \sigma_\theta + v \cos \theta q_y \sigma_x, \quad (3)$$

where $v = \frac{\sqrt{3}}{4}\sqrt{|1 - \beta^2|}dt_L$, the angle $\theta \in [0, \pi/2]$ is defined as $\tan \theta = \sqrt{1 - \beta^2}/\sqrt{3}\beta$ (with $\theta \rightarrow \pi - \theta$ for the other Dirac point), and $\sigma_\theta = \boldsymbol{\sigma} \cdot \mathbf{u}_\theta$, with $\mathbf{u}_\theta = -\sin \theta \mathbf{u}_y + \cos \theta \mathbf{u}_z$, where $\mathbf{u}_{x,y,z}$ are Cartesian unit vectors. Analogously, for $\beta > 1$, around a type-III Dirac point ($E_D = E_0 - \frac{3}{2}t_L$), the reduced Hamiltonian reads:

$$H(\mathbf{q}) = v \cos \phi q_y \sigma_0 + v q_x \sigma_\phi - v \cos \phi q_y \sigma_z, \quad (4)$$

where $\tan \phi = \sqrt{\beta^2 - 1}/\sqrt{4 - \beta^2}$ and $\sigma_\phi = \boldsymbol{\sigma} \cdot \mathbf{u}_\phi$, with $\mathbf{u}_\phi = \cos \phi \mathbf{u}_x - \sin \phi \mathbf{u}_y$ (for the other Dirac point: $\phi \rightarrow \pi - \phi$). By comparing $H(\mathbf{q})$ in Eqs. 3 and 4 with the generalised Dirac Hamiltonian, we can directly extract the Dirac effective velocities as a function of β (shown as solid lines in Fig. 3f for v_{0x} and v_x) as well as the tilt parameter \tilde{v}_0 :

	$ v_{0x} $	$ v_{0y} $	$ v_x $	$ v_y $	\tilde{v}_0
$\beta < 1$	$v \cos \theta$	0	v	$v \cos \theta$	$\cos \theta$
$\beta > 1$	0	$v \cos \phi$	v	$v \cos \phi$	1

To compute the winding of the Dirac cones, Hamiltonians 3 and 4 can be rearranged similarly to the rightmost hand side of Eq. 2, with a term in the form $\mathbf{h}(\mathbf{q}) \cdot \boldsymbol{\sigma}$. For $\beta < 1$ (Hamiltonian 3), the winding of $\mathbf{h}(\mathbf{q})$ around each of the Dirac cones is $\mathcal{W} = 1$, as indicated in the right panels of Fig. 3. This is also the case for the type-III Dirac cones for $\beta > 1$ (winding of Hamiltonian 4). A prominent feature of these Hamiltonians is that the vector $\mathbf{h}(\mathbf{q})$ winds on a plane that depends on the deformation β , namely on the plane $(\mathbf{u}_x, \mathbf{u}_\theta)$ for $\beta < 1$, and $(\mathbf{u}_\phi, \mathbf{u}_z)$ for $\beta > 1$ (see Supplementary Information).

The analysis of the windings sheds light on the mechanisms behind the creation of Dirac cones starting from a flat band touching a dispersive band. The single band touching at $\beta = 1$ is described by a winding $\mathcal{W} = 2$. When $\beta \leq 1$ the band touching evolves into a pair of Dirac cones (tilted or type-III) with winding $\mathcal{W} = 1$. This is an illustration of one of the two possible scenarios for Dirac merging in two dimension, characteristic of, for example, bilayer graphene³⁷. Remarkably, the orbital p-bands show the two possible universal scenarios for the merging of Dirac cones in two dimensions³⁹: (i) two Dirac cones with $\mathcal{W} = 1$ emerge from a point with $\mathcal{W} = 2$, observed in the lower part of the spectra of Fig. 3; (ii) two Dirac cones with opposite winding $\mathcal{W} = \pm 1$ merge in a semi-Dirac cone with $\mathcal{W} = 0$, reported in the central part of the spectra in Fig. 3 (a 2×2 effective Hamiltonian analysis can also be done for the Dirac points at E_0).

The photonic realisation here reported demonstrates the flexibility of orbital bands to implement unconventional Dirac points. This is an asset for the engineering of photonic materials that combine different types of Dirac dispersions, an promising configuration for the study of analogue black holes in photonics^{21,40}. Moreover, our experiments provide a recipe for the implementation of Dirac cones

in solid state materials: the touching of a flat and a dispersive band with winding $\mathcal{W} = 2$ evolves into two Dirac cones in the presence of strain. This behaviour has been predicted for other lattice geometries³⁶, and it presents a natural playground to investigate the transition between different topological phases when particle interactions are present^{41,42} or when time reversal symmetry is broken. Polaritons are particularly well suited to study these scenarios: thanks to their excitonic component they present significant repulsive interactions in the high density regime⁴³ and they are sensitive to external magnetic fields, allowing the implementation of quantum Hall phases^{44,45}. Polariton orbital bands of the kind here reported open exciting perspectives for the study of topological lasers⁴⁶ and of Dirac superfluids⁴⁷.

Acknowledgements. This work was supported by the ERC grant HoneyPol, the EU-FET Proactive grant AQUoS, the French National Research Agency (ANR) project Quantum Fluids of Light (ANR-16-CE30-0021) and the Labex CEMPI (ANR-11-LABX-0007) and NanoSaclay (ICQOQS, Grant No. ANR-10-LABX-0035), the French RENATECH network, the CPER Photonics for Society P4S, and the Métropole Européenne de Lille via the project TFlight. T.O. acknowledges support from the Interdisciplinary Theoretical and Mathematical Sciences Program (iTHEMS) at RIKEN

References

1. Castro Neto, A. H., Guinea, F., Peres, N. M. R., Novoselov, K. S. & Geim, A. K. The electronic properties of graphene. *Rev. Mod. Phys.* **81**, 109–162 (2009).
2. Zhao, Y. *et al.* Creating and probing electron whispering-gallery modes in graphene. *Science* **348**, 672–675 (2015).
3. Bernevig, B. A. & Hughes, T. L. *Topological Insulators and Topological Superconductors*. (Princeton University Press, 2013).
4. Montambaux, G., Piéchon, F., Fuchs, J.-N. & Goerbig, M. Merging of Dirac points in a two-dimensional crystal. *Phys. Rev. B* **80**, 153412 (2009).
5. Lim, L.-K., Fuchs, J.-N. & Montambaux, G. Bloch-Zener Oscillations across a Merging Transition of Dirac Points. *Phys. Rev. Lett.* **108**, 175303 (2012).
6. Tarruell, L., Greif, D., Uehlinger, T., Jotzu, G. & Esslinger, T. Creating, moving and merging Dirac points with a Fermi gas in a tunable honeycomb lattice. *Nature* **483**, 302–305 (2012).
7. Bellec, M., Kuhl, U., Montambaux, G. & Mortessagne, F. Topological Transition of Dirac Points in a Microwave Experiment. *Phys. Rev. Lett.* **110**, 033902 (2013).
8. Rechtsman, M. C. *et al.* Topological Creation and Destruction of Edge States in Photonic Graphene. *Phys. Rev. Lett.* **111**, 103901 (2013).
9. Kim, J. *et al.* Observation of tunable band gap and anisotropic Dirac semimetal state in black phosphorus. *Science* **349**, 723–726 (2015).
10. Goerbig, M. O., Fuchs, J.-N., Montambaux, G. & Piéchon, F. Tilted anisotropic Dirac cones in quinoid-type graphene and α -(BEDT-TTF)₂I₃. *Phys. Rev. B* **78**, 45415 (2008).
11. Lu, H.-Y. *et al.* Tilted anisotropic Dirac cones in partially hydrogenated graphene. *Phys. Rev. B* **94**, 195423 (2016).
12. Katayama, S., Kobayashi, A. & Suzumura, Y. Pressure-Induced Zero-Gap Semiconducting State in Organic Conductor α -(BEDT-TTF)₂I₃ Salt. *J. Phys. Soc. Japan* **75**, 54705 (2006).
13. Hirata, M. *et al.* Observation of an anisotropic Dirac cone reshaping and ferrimagnetic spin polarization in an organic conductor. *Nat. Commun.* **7**, 12666 (2016).
14. Nguyen, V. H. & Charlier, J.-C. Klein tunneling and electron optics in Dirac-Weyl fermion systems with tilted energy dispersion. *arXiv:1711.06602* (2017).
15. Chan, C.-K., Lindner, N. H., Refael, G. & Lee, P. A. Photocurrents in Weyl semimetals. *Phys. Rev. B* **95**, 41104 (2017).
16. Soluyanov, A. A. *et al.* Type-II Weyl semimetals. *Nature* **527**, 495–498 (2015).
17. Deng, K. *et al.* Experimental observation of topological Fermi arcs in type-II Weyl semimetal MoTe₂. *Nat. Phys.* **12**, 1105 (2016).
18. Huang, L. *et al.* Spectroscopic evidence for a type II Weyl semimetallic state in MoTe₂. *Nat. Mater.* **15**, 1155 (2016).
19. Noh, H.-J. *et al.* Experimental Realization of Type-II Dirac Fermions in a PdTe₂ Superconductor. *Phys. Rev. Lett.* **119**, 016401 (2017).

20. Nissinen, J. & Volovik, G. E. Type-III and IV interacting Weyl points. *JETP Lett.* **105**, 447–452 (2017).
21. Huang, H., Jin, K.-H. & Liu, F. Black Hole Horizon in a Type-III Dirac Semimetal $\text{Zn}_2\text{In}_2\text{S}_5$. *arXiv:1711.07096* (2017).
22. Li, D., Rosenstein, B., Shapiro, B. Y. & Shapiro, I. Effect of the type-I to type-II Weyl semimetal topological transition on superconductivity. *Phys. Rev. B* **95**, 94513 (2017).
23. Leykam, D., Andreanov, A. & Flach, S. Artificial flat band systems: from lattice models to experiments. *Adv. Phys. X* **3**, 1473052 (2018).
24. Amo, A. & Bloch, J. Exciton-polaritons in lattices: A non-linear photonic simulator. *Comptes Rendus Phys.* **17**, (2016).
25. Pyrialakos, G. G., Nye, N. S., Kantartzis, N. V. & Christodoulides, D. N. Emergence of Type-II Dirac Points in Graphynelike Photonic Lattices. *Phys. Rev. Lett.* **119**, 113901 (2017).
26. Mann, C.-R., Sturges, T. J., Weick, G., Barnes, W. L. & Mariani, E. Manipulating type-I and type-II Dirac polaritons in cavity-embedded honeycomb metasurfaces. *Nat. Commun.* **9**, 2194 (2018).
27. Yang, B. *et al.* Ideal Weyl points and helicoid surface states in artificial photonic crystal structures. *Science* 10.1126/eaq1221 (2018).
28. Hu, C. *et al.* Type-II Dirac Photons at Metasurfaces. *Phys. Rev. Lett.* **121**, 24301 (2018).
29. Jiho Noh *et al.* Experimental observation of optical Weyl points and Fermi arc-like surface states. *Nat. Phys.* **13**, 611–617 (2017).
30. Jacqmin, T. *et al.* Direct Observation of Dirac Cones and a Flatband in a Honeycomb Lattice for Polaritons. *Phys. Rev. Lett.* **112**, 116402 (2014).
31. Milićević, M. *et al.* Orbital Edge States in a Photonic Honeycomb Lattice. *Phys. Rev. Lett.* **118**, 107403 (2017).
32. Milićević, M. *et al.* Edge states in polariton honeycomb lattices. *2D Mater.* **2**, 034012 (2015).
33. Shirley, E. L., Terminello, L. J., Santoni, A. & Himpsel, F. J. Brillouin-zone-selection effects in graphite photoelectron angular distributions. *Phys. Rev. B* **51**, 13614–13622 (1995).
34. Wu, C., Bergman, D., Balents, L. & Das Sarma, S. Flat Bands and Wigner Crystallization in the Honeycomb Optical Lattice. *Phys. Rev. Lett.* **99**, 070401 (2007).
35. Galbiati, M. *et al.* Polariton Condensation in Photonic Molecules. *Phys. Rev. Lett.* **108**, 126403 (2012).
36. Montambaux, G., Lim, L.-K., Fuchs, J.-N. & Piéchon, F. Winding vector: how to annihilate two Dirac points with the same charge. *arXiv:1804.00781* (2018).
37. Chong, Y. D., Wen, X.-G. & Soljačić, M. Effective theory of quadratic degeneracies. *Phys. Rev. B* **77**, 235125 (2008).
38. Cohen-Tannoudji, C., Grynberg, J. & Dupont-Roc, G. *Atom-Photon Interactions: Basic Process and Applications*. (Wiley, 1992).
39. de Gail, R., Fuchs, J.-N., Goerbig, M. O., Piéchon, F. & Montambaux, G. Manipulation of Dirac points in graphene-like crystals. *Phys. B Condens. Matter* **407**, 1948–1952 (2012).
40. Volovik, G. E. Black hole and hawking radiation by type-II Weyl fermions. *JETP Lett.* **104**, 645–648 (2016).
41. Dóra, B., Herbut, I. F. & Moessner, R. Occurrence of nematic, topological, and Berry phases when a flat and a parabolic band touch. *Phys. Rev. B* **90**, 45310 (2014).
42. Sun, K., Yao, H., Fradkin, E. & Kivelson, S. A. Topological Insulators and Nematic Phases from Spontaneous Symmetry Breaking in 2D Fermi Systems with a Quadratic Band Crossing. *Phys. Rev. Lett.* **103**, 46811 (2009).
43. Carusotto, I. & Ciuti, C. Quantum fluids of light. *Rev. Mod. Phys.* **85**, 299–366 (2013).
44. Nalitov, A. V., Solnyshkov, D. D. & Malpuech, G. Polariton Z Topological Insulator. *Phys. Rev. Lett.* **114**, 116401 (2015).
45. Karzig, T., Bardyn, C.-E., Lindner, N. H. & Refael, G. Topological Polaritons. *Phys. Rev. X* **5**, 031001 (2015).
46. St-Jean, P. *et al.* Lasing in topological edge states of a one-dimensional lattice. *Nat. Photonics* **11**, 651–656 (2017).
47. Di Liberto, M., Hemmerich, A. & Morais Smith, C. Topological Varma Superfluid in Optical Lattices. *Phys. Rev. Lett.* **117**, 163001 (2016).

Supplementary Information

Tilted and type-III Dirac cones emerging from flat bands in photonic orbital graphene

M. Milicevic¹, G. Montambaux², T. Ozawa³, I. Sagnes¹, A. Lemaître¹, L. Le Gratiet¹, A. Harouri¹, J. Bloch¹, A. Amo⁴

¹Centre de Nanosciences et de Nanotechnologies, CNRS, Univ. Paris-Sud, Université Paris-Saclay, C2N-Marcoussis, 91460 Marcoussis, France

²Laboratoire de Physique des Solides, CNRS, Univ. Paris-Sud, Université Paris-Saclay, 91405 Orsay Cedex, France

³Interdisciplinary Theoretical and Mathematical Sciences Program (iTHEMS), RIKEN, Wako, Saitama 351-0198, Japan

⁴Univ. Lille, CNRS, UMR 8523 – PhLAM – Physique des Lasers Atomes et Molécules, F-59000 Lille, France

Content :

I.- Sample description and experimental set-up.....	11
II.- Tight-binding Hamiltonian and extraction of β	13
III.- Gap opening at $\beta = 0.45$	15
IV.- Tomography of tilted Dirac cones	16
V.- Measurement and calculation of the effective Dirac velocities	17
VI.- Hamiltonian reduction and winding around the band touching points	18

I.- Sample description and experimental set-up

The sample used in the experiments is a semiconductor microcavity grown by molecular beam epitaxy. Two Bragg mirrors made of 28 (top) and 40 (bottom) pairs of $\lambda/4$ alternating layers of $\text{Ga}_{0.05}\text{Al}_{0.95}\text{As}/\text{Ga}_{0.80}\text{Al}_{0.20}\text{As}$ embed a $\lambda/2$ $\text{Ga}_{0.80}\text{Al}_{0.20}\text{As}$ cavity. $\lambda = 775$ nm is the emission/absorption wavelength of free excitons of 12 GaAs, 7 nm wide quantum wells grown in groups of four in the three central maxima of the electromagnetic field of the cavity. At 10 K, the temperature of the experiments, the excitonic and photonic resonances are in the strong coupling regime, with a Rabi splitting of 15 meV. The experiments are performed at a photon-exciton detuning of -10 meV (measured at the energy of the lowest energy flat band), except for the data shown in Fig. 3c, for which the detuning is -2 meV.

To fabricate the honeycomb lattices, the as-grown planar structure is subject to e-beam lithography and Inductively Coupled Plasma etching down to the GaAs substrate. Each micropillar in the lattice has a diameter of 2.75 μm , and the centre-to-centre distance varies between 2.4 and 2.72 μm , ensuring the overlap between adjacent micropillars. The polariton lifetime measured in a similar unetched

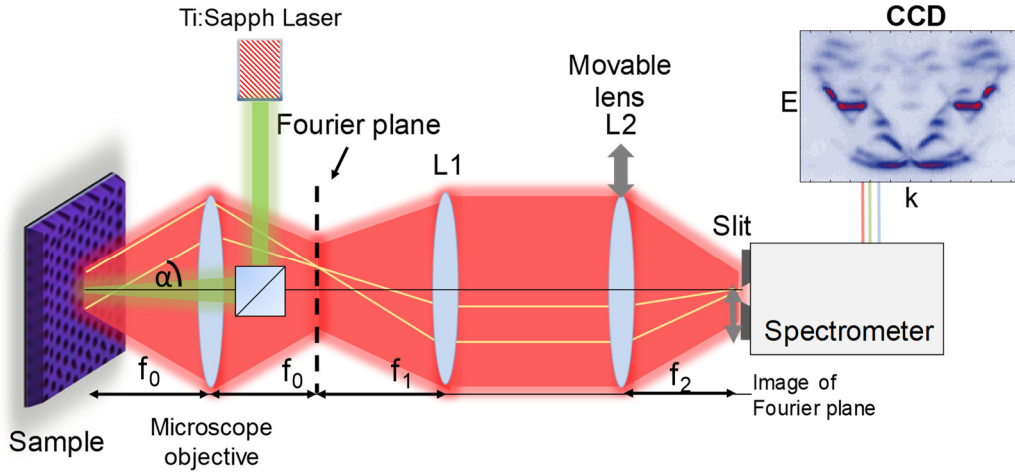


Figure S1. Experimental setup. Sketch of the experimental set-up employed to measure the momentum and energy resolved photoluminescence. Lenses L1 and L2 image the Fourier plane of the microscope objective on the entrance slit of the spectrometer, resulting in a k_x vs energy image for a fixed value of k_y . By moving laterally lens L2 different values of k_y can be accessed.

microcavity is of the order of 30 ps. In the etched structures, the lateral defects induced during the microfabrication process reduce the lifetime to about 3-5 ps.

Experiments are performed by exciting the centre of each lattice with a continuous wave laser focalised in a spot of 3 μm in diameter (full width at half maximum). The wavelength of the laser is 745 nm (1.6642 eV), corresponding to an energy about 100 meV above the lower polariton s- and p-bands. The laser injects electron and holes that relax down incoherently to form polaritons that populate the lower bands of the lattice. The photons that escape out of the sample conserve the energy and in-plane momentum of polaritons in the lattice. The latter is related to the angle of emission following the expression: $k_{\parallel} = \frac{E}{\hbar c} \sin(\alpha)$, where α is the emission angle measured from the normal to the lattice plane, E is the energy of the emitted photon and c is the speed of light in vacuum. Therefore, by resolving the emission in energy and in angle we can measure the polariton dispersion.

Figure S1 shows the experimental set-up, in which the Fourier plane of the excitation/collection lens (microscope objective) is imaged on the entrance slit of a spectrometer attached to a CCD. We select the emission linearly polarized along the k_y direction, parallel to the grooves of the grating in the spectrometer. Similar results were obtained for the perpendicular polarisation.

A single image of the CCD registers the emission energy as a function of k parallel to the entrance slit (as shown in the figure), for a fixed value of k perpendicular to the entrance slit of the spectrometer. By taking images for different lateral positions of lens L2, we can perform a full tomography of the three-dimensional space “energy, k_x, k_y ”. Post-processing of the data allows displaying energy-momentum cuts along any momentum direction or momentum-momentum cuts for a given emission energy.

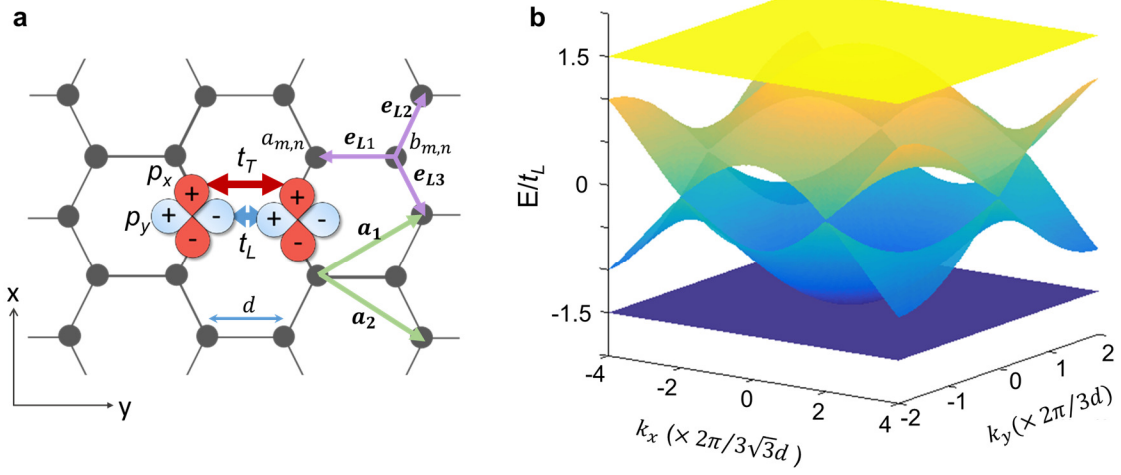


Figure S2. Tight-binding dispersions. **a** Scheme of the honeycomb lattice and the unit vectors used in the tight binding model. **b** Spectrum of the p-bands obtained from the diagonalization of Hamiltonian E2 with $t_T = 0$ and $\beta = 1$.

II.- Tight-binding Hamiltonian and extraction of β

The coupling of the p_x , p_y orbitals in the isotropic honeycomb lattice can be described by a tight-binding Hamiltonian of the form^{1,2}:

$$H = - \sum_{m,n} \{ t_L (\hat{a}_{m,n}^\dagger \cdot \mathbf{e}_{L1}) (\mathbf{e}_{L1} \cdot \hat{b}_{m,n}) + t_L (\hat{a}_{m+1,n}^\dagger \cdot \mathbf{e}_{L2}) (\mathbf{e}_{L2} \cdot \hat{b}_{m,n}) + t_L (\hat{a}_{m,n+1}^\dagger \cdot \mathbf{e}_{L3}) (\mathbf{e}_{L3} \cdot \hat{b}_{m,n+1}) + t_T (\hat{a}_{m,n}^\dagger \cdot \mathbf{e}_{T1}) (\mathbf{e}_{T1} \cdot \hat{b}_{m,n}) + t_T (\hat{a}_{m+1,n}^\dagger \cdot \mathbf{e}_{T2}) (\mathbf{e}_{T2} \cdot \hat{b}_{m,n}) + t_T (\hat{a}_{m,n+1}^\dagger \cdot \mathbf{e}_{T3}) (\mathbf{e}_{T3} \cdot \hat{b}_{m,n+1}) + h.c. \}, \quad (E1)$$

where, $\mathbf{e}_{L1,L2,L3}$ are unit vectors oriented parallel to the nearest-neighbour links of each site (see Fig. S2a), $\mathbf{e}_{T1,T2,T3}$ are unit vectors oriented perpendicular to $\mathbf{e}_{L1,L2,L3}$, respectively, $\hat{a}_{m,n}^\dagger = (\hat{a}_{m,n}^\dagger(x), \hat{a}_{m,n}^\dagger(y))$ and $\hat{b}_{m,n}^\dagger = (\hat{b}_{m,n}^\dagger(x), \hat{b}_{m,n}^\dagger(y))$, with $\hat{a}_{m,n}^\dagger(x,y)$, $\hat{b}_{m,n}^\dagger(x,y)$ the creation operators of a photon in the p_x or p_y orbital of the a , b site of the m, n unit cell in the lattice. If the hopping of orbitals oriented perpendicular to the links is negligible ($t_T = 0$), Hamiltonian E1 can be written in momentum space in the form²:

$$H(\mathbf{k}) = -t_L \begin{pmatrix} 0_{2 \times 2} & Q(\mathbf{k}) \\ Q(\mathbf{k})^\dagger & 0_{2 \times 2} \end{pmatrix}, \text{ with } Q(\mathbf{k}) = \begin{pmatrix} f_1 & g \\ g & f_2 \end{pmatrix}, \quad (E2)$$

where $f_1 = \frac{3}{4}(e^{ik \cdot \mathbf{a}_1} + e^{ik \cdot \mathbf{a}_2})$, $f_2 = 1 + \frac{1}{4}(e^{ik \cdot \mathbf{a}_1} + e^{ik \cdot \mathbf{a}_2})$, and $g = \frac{\sqrt{3}}{4}(e^{ik \cdot \mathbf{a}_1} - e^{ik \cdot \mathbf{a}_2})$, with $\mathbf{a}_1 = (\frac{\sqrt{3}}{2}d, \frac{3}{2}d)$, $\mathbf{a}_2 = (-\frac{\sqrt{3}}{2}d, \frac{3}{2}d)$ the lattice vectors depicted in Fig. S2a and $\mathbf{k} = (k_x, k_y)$ the quasi-momentum. The diagonalization of Hamiltonian E2 results in four bands depicted in Fig. S2b. The

spectrum shows two flat bands at high and low energy that touch two dispersive bands with six Dirac points (only two are non-equivalent).

If we account for different hoppings t_L and t'_L for different links, Hamiltonian E2 is still valid with the same expressions for f_1 and g , and f_2 replaced by $f_2 = \beta + \frac{1}{4}(e^{ik \cdot a_1} + e^{ik \cdot a_2})$. As a function of $\beta = t'_L/t_L$, its spectrum $\varepsilon(\mathbf{k})$ takes the form:

$$\varepsilon(\mathbf{k}) = \pm \sqrt{E_0(\mathbf{k}) \pm E(\mathbf{k})} \quad (\text{E3})$$

where the four sign combinations make the four bands and:

$$E(\mathbf{k}) = t_L \left[\frac{3}{4} \sin^2(K_x) \cdot (\beta^2 + \cos^2(K_x) - 2\beta \cos(K_x) \cos(K_y)) + \frac{1}{4} (2\cos^2(K_x) - \beta^2 - \beta \cos(K_x) \cos(K_y))^2 \right]^{1/2}, \quad (\text{E4})$$

$$E_0(\mathbf{k}) = \frac{t_L}{4} (3 + 2\beta^2 + 2\cos^2(K_x) + 2\beta \cos(K_x) \cos(K_y)), \quad (\text{E5})$$

with $K_x \equiv \frac{\sqrt{3}}{2} k_x d$ and $K_y \equiv \frac{3}{2} k_y d$.

For $\beta < 1$ the energy E_D and momentum space coordinates of the low energy emerging Dirac cones are:

$$E_D = E_0 - \frac{1}{2} \sqrt{3 + 6\beta^2} t_L, K_y = 0, \cos K_x = \beta, \quad (\text{E6a})$$

while for $\beta > 1$ they are:

$$E_D = E_0 - \frac{3}{2} t_L, \cos K_y = \frac{2-\beta^2}{\beta} 0, K_x = 0, \quad (\text{E6b})$$

In Figs. 3 and 4 of the main text, the experimental value of β is obtained from fits of the spectrum of the tight-binding model to the measured dispersions, in which $t_T = 0$ and t_L , β and the onsite energy E_0 are the fitting parameters.

III.- Gap opening at $\beta = 0.45$

Figure 3c of the main text shows the formation of a semi-Dirac cone at $E = E_0$ for $\beta = 0.5$. If β is further reduced to 0.45, a gap opens. To further evidence the gap opening, Fig. S3 shows the spectrum obtained from Figs. 3c and d at the momentum of the Dirac point ($k_x = -3 \times 2\pi/3\sqrt{3}d$) for $\beta = 0.5$ and $\beta = 0.45$. In the latter case a splitting is apparent at E_0 , corresponding to the gap opening.

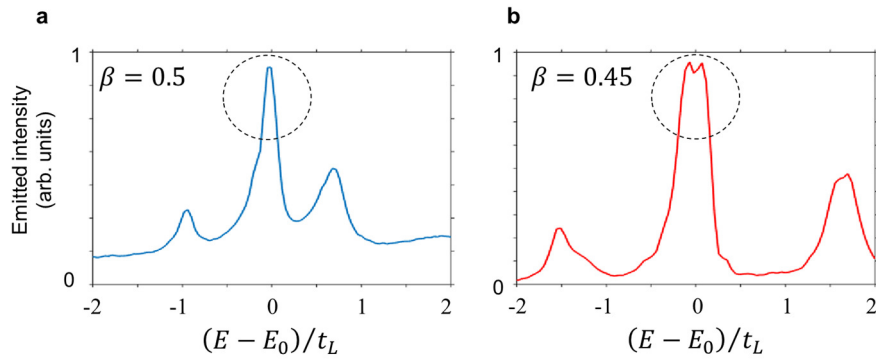


Figure S3. Spectrum at gap opening. **a, b** Photoluminescence spectra taken at the momentum position of the semi-Dirac cone $k_x = -3 \times 2\pi/3\sqrt{3}d$, $k_y = 2\pi/(d' + d/2)$, for $\beta = 0.5$ (**a**) and $\beta = 0.45$ (**b**), corresponding to Fig. 3c and d, respectively. In **b**, a splitting is apparent in the circled area.

IV.- Tomography of tilted Dirac cones

Figure 3 of the main text shows the emergence of tilted Dirac cones from the flat band – dispersive band touching when $\beta < 1$. The tilt is clearly visible in the k_x direction, resulting in a non-zero value of v_{0x} (as defined in Eq. 1). Figure S4 shows the dispersion across one of the newly created Dirac cones in the k_y direction for $\beta = 0.5$. The white solid lines depict the eigenvalues calculated by diagonalising Hamiltonian E2. As it is apparent from the measured spectra and the tight-binding bands, the newly created cones are not tilted along the k_y direction, resulting in $v_{0y} \approx 0$.

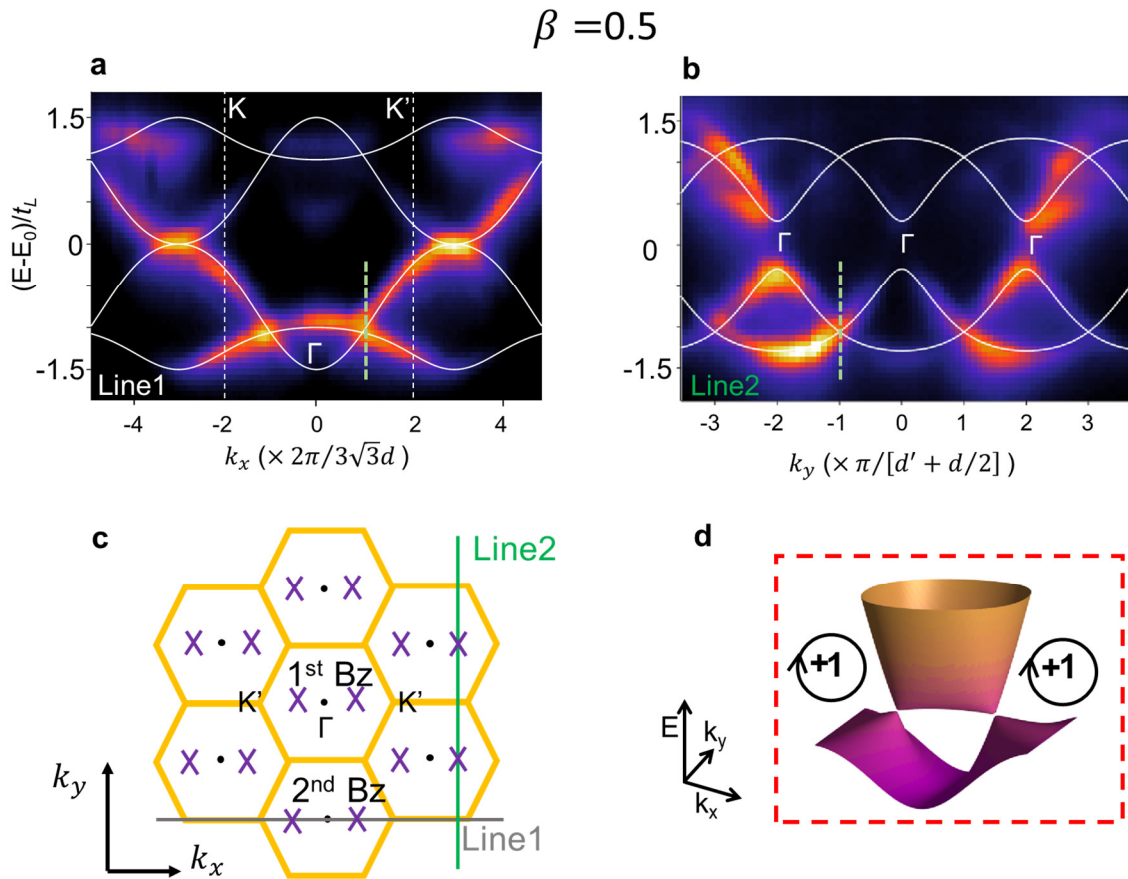


Figure S4. Tomography of tilted Dirac cones. **a** Measured dispersion along the k_x direction for $k_y = 4\pi/(d' + d/2)$ (line 1 in panel **c**) for $\beta = 0.5$ (same as Fig. 3c). **b** Measured dispersion along the k_y direction for $k_x = 2\pi/3\sqrt{3}d$, traversing the tilted Dirac cone (green dashed line in **a**, line 2 in **c**). **c** Sketch of the different Brillouin zones in momentum space. The orange hexagons show the Brillouin zones as defined for $\beta = 1$. The crosses indicate the position of the emergent tilted Dirac cones. **d** Zoom of the tight-binding eigenenergies in the region close to the lowest energy Dirac points. Parameters are the same as for Fig. 3c.

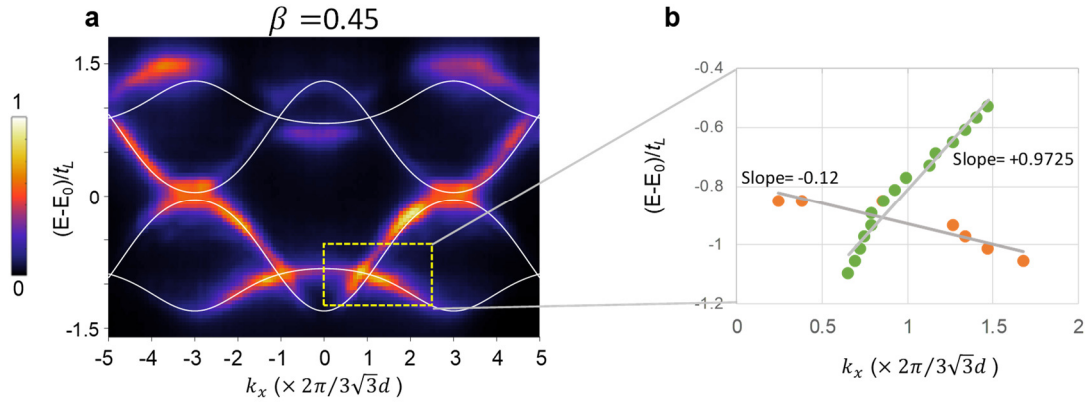


Figure S5. **a** Measured dispersion along the k_x direction for $k_y = 2\pi/(d' + d/2)$ for $\beta = 0.45$ (same as Fig. 3d). **b** Extracted data points from the Dirac point marked in a dashed rectangle in **a**. From linear fits to the points we obtain $|v_{0x}|$ and $|v_x|$, plotted in Fig. 3f of the main text.

V.- Measurement and calculation of the effective Dirac velocities

Figure 3f of the main text shows the effective Dirac velocities v_{0x} and v_x measured from the measured dispersions along the k_x direction plotted in Fig. 3. To measure these velocities, we first extract the dispersion around the Dirac cones from the maximum photoluminescence intensity as a function of energy and momentum. For the case of $\beta = 0.45$, the data points are shown in Fig. S5b. A linear fit allows measuring the slope of the dispersion. By comparison with Eq. 1 of the main text, the two measured slopes correspond to $|v_{0x}| - |v_x|$ and $|v_{0x}| + |v_x|$. From that, we extract $|v_{0x}|$ and $|v_x|$. We repeat the procedure for the symmetric Dirac point and we take the average of their absolute value.

Note that for type-I Dirac cones, $v_{0x} = v_{0y} = 0$, and the absolute value of the two slopes should be identical and equal to v_x . To test this hypothesis, we have measured the slope around the K' type-I Dirac cone at E_0 in Fig. 3a at positive momenta. After converting the slopes to effective Weyl velocities (Eq. 1 of the main text) we obtain $|v_{0x}| = 0.07 \pm 0.03$ and $|v_x| = 0.72 \pm 0.03$ in units of dt_L .

From the tight-binding Hamiltonian, the effective Dirac velocities can be obtained from the derivative along k_x and k_y of the eigenvalues of E3-E5 at the position of the emergent Dirac cones (E6), resulting in the analytical expressions for $\beta < 1$ (normalised to dt_L , where we have assumed that in the experiment $d \approx d'$):

$$|v_{0x}| = \frac{3\beta}{4} \sqrt{\frac{1-\beta^2}{1+2\beta^2}}, \quad |v_{0y}| = 0, \quad |v_x| = \frac{\sqrt{3}}{4} \sqrt{1-\beta^2}, \quad |v_y| = \frac{\sqrt{3-3\beta^2}}{4}. \quad (\text{E7})$$

The analytical expressions for $|v_{0x}|$ and $|v_x|$ are shown in solid lines in Figs. S5 and 3f.

For $1 < \beta < 2$ we have (same units as above):

$$|v_{0x}| = 0, \quad |v_{0y}| = |v_y| = \frac{1}{4} \sqrt{(\beta^2 - 1)(4 - \beta^2)}, \quad |v_x| = \frac{\sqrt{3}}{4} \sqrt{\beta^2 - 1}. \quad (\text{E8})$$

Note that the fact that $|v_{0y}| = |v_y|$ (with opposite sign: $v_{0y} = -v_y$) for $\beta > 1$ is the signature of the type-III Dirac cone, and it results in a flat band along the k_y direction.

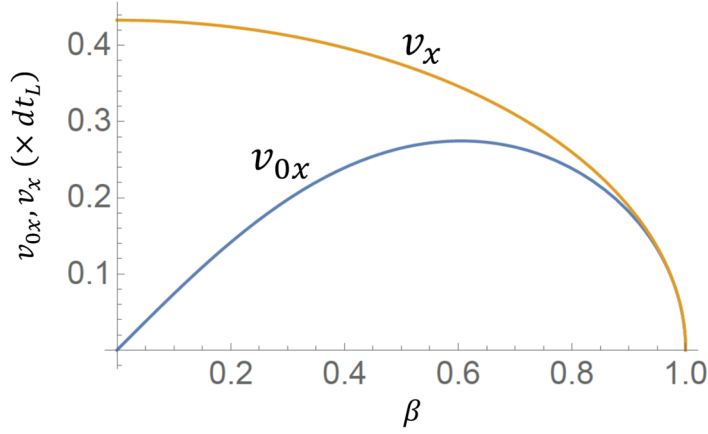


Figure S5. v_{0x} and v_x as a function of β calculated from the derivative of the tight-binding spectrum at the position of the emergent Dirac cones.

VI.- Hamiltonian reduction and winding around the band touching points

The vicinity of touching point between two bands can be described by an effective 2×2 Hamiltonian obtained from the projection of the full 4×4 Hamiltonian on the subspace of the two lowest energy bands³. The reduced Hamiltonian can be expressed in the generic form:

$$H(\mathbf{q}) = \alpha(\mathbf{q})\sigma_0 + \mathbf{h}(\mathbf{q}) \cdot \boldsymbol{\sigma} = \alpha(\mathbf{q})\sigma_0 + h_a(\mathbf{q}) \cdot \sigma_a + h_b(\mathbf{q}) \cdot \sigma_b, \quad (\text{E9})$$

where σ_0 is the 2×2 identity matrix and $\sigma_{a,b} = \mathbf{u}_{a,b} \cdot \boldsymbol{\sigma}$, with $\mathbf{u}_{a,b}$ unit vectors and $\boldsymbol{\sigma} = (\sigma_x, \sigma_y, \sigma_z)$ is the vector of Pauli matrices. Without loss of generality and for simplicity, we consider the case of $\mathbf{u}_a \cdot \mathbf{u}_b = 0$, which implies $\{\sigma_a, \sigma_b\} = 0$.

The winding vector of this Hamiltonian around the band touching point is⁴:

$$\mathcal{W} = \frac{1}{2\pi} \oint \mathbf{n}(\mathbf{q}) \times d\mathbf{n}(\mathbf{q}) = \frac{\mathbf{u}_c}{2\pi} \oint \frac{h_a(\mathbf{q})\nabla h_b(\mathbf{q}) - h_b(\mathbf{q})\nabla h_a(\mathbf{q})}{h_a^2(\mathbf{q}) + h_b^2(\mathbf{q})} d\mathbf{q}, \quad (\text{E10})$$

where $\mathbf{u}_c = \mathbf{u}_a \times \mathbf{u}_b$ and $\mathbf{n}(\mathbf{q}) = \frac{\mathbf{h}(\mathbf{q})}{|\mathbf{h}(\mathbf{q})|}$. The integral is performed along a closed line in momentum space that encircles the band touching point. The modulus of \mathcal{W} can only take integer values.

The effective 2×2 Hamiltonian described in the main text close to the flat-parabolic touching at the Γ point for $\beta = 1$ takes the form:

$$H(\mathbf{q}) = -\frac{3}{2}t_L\sigma_0 + \frac{3}{8}t_L \begin{pmatrix} q_x^2 & q_x q_y \\ q_x q_y & q_y^2 \end{pmatrix} \equiv -\frac{3}{2}t_L\sigma_0 + \mathbf{h}(\mathbf{q}) \cdot \boldsymbol{\sigma}, \quad (\text{E11})$$

and it is characterized by the winding vector $\mathcal{W} = +2 \mathbf{u}_z$.

For $\beta < 1$, close to the emerging Dirac cone, it reads:

$$H(\mathbf{q}) = v \cos \theta q_x \sigma_0 + v q_x \sigma_\theta + v \cos \theta q_y \sigma_x, \quad (\text{E12})$$

where $v = \frac{\sqrt{3}}{4} \sqrt{|1 - \beta^2|} dt_L$, the angle $\theta \in [0, \pi/2]$ is defined as $\tan \theta = \sqrt{1 - \beta^2} / \sqrt{3} \beta$ (with $\theta \rightarrow \pi - \theta$ for the other Dirac cone), and $\sigma_\theta = \boldsymbol{\sigma} \cdot \mathbf{u}_\theta$, with $\mathbf{u}_\theta = -\sin \theta \mathbf{u}_y + \cos \theta \mathbf{u}_z$, where $\mathbf{u}_{x,y,z}$ are Cartesian unit vectors.

Analogously, for $\beta > 1$, around one of the type-III Dirac points, the reduced Hamiltonian reads:

$$H(\mathbf{q}) = v \cos \phi q_y \sigma_0 + v q_x \sigma_\phi - v \cos \phi q_y \sigma_z, \quad (\text{E13})$$

where $\tan \phi = \sqrt{\beta^2 - 1} / \sqrt{4 - \beta^2}$ and $\sigma_\phi = \boldsymbol{\sigma} \cdot \mathbf{u}_\phi$, with $\mathbf{u}_\phi = \cos \phi \mathbf{u}_x - \sin \phi \mathbf{u}_y$ (for the other Dirac point: $\phi \rightarrow \pi - \phi$).

By comparing the form of Eqs. E12 and E13 with the generalised Dirac Hamiltonian presented in the main text and its eigenvalues in Eq. 1, we can write the effective velocities and tilt parameter \tilde{v}_0 as a function of v , θ and ϕ :

	$ v_{0x} $	$ v_{0y} $	$ v_x $	$ v_y $	$\tilde{v}_0 = \sqrt{\left(\frac{v_{0x}}{v_x}\right)^2 + \left(\frac{v_{0y}}{v_y}\right)^2}$
$\beta < 1$	$v \cos \theta$	0	v	$v \cos \theta$	$\cos \theta$
$\beta > 1$	0	$v \cos \phi$	v	$v \cos \phi$	1

If v , θ and ϕ are explicitly expressed in terms of β we obtain Eqs. E7 and E9, in agreement with the full tight-binding calculation.

The modulus of the winding vector for Hamiltonian E11 is $\mathcal{W} = 2$, while for each of the tilted ($\beta < 1$) and type-III Dirac cones ($\beta > 1$), the winding is $\mathcal{W} = 1$. As stated in the main text, a prominent feature of these Hamiltonians is that vector $\mathbf{h}(\mathbf{q})$ winds on a plane whose orientation depends on the deformation β . Namely, for $\beta < 1$ the pseudo-field $\mathbf{h}(\mathbf{q})$ resides on the plane $(\mathbf{u}_x, \mathbf{u}_\theta)$ and the winding vector points in the direction $\frac{\mathbf{w}}{|\mathbf{w}|} = (0, \cos \theta, \pm \sin \theta)$. The winding vector plane thus rotates

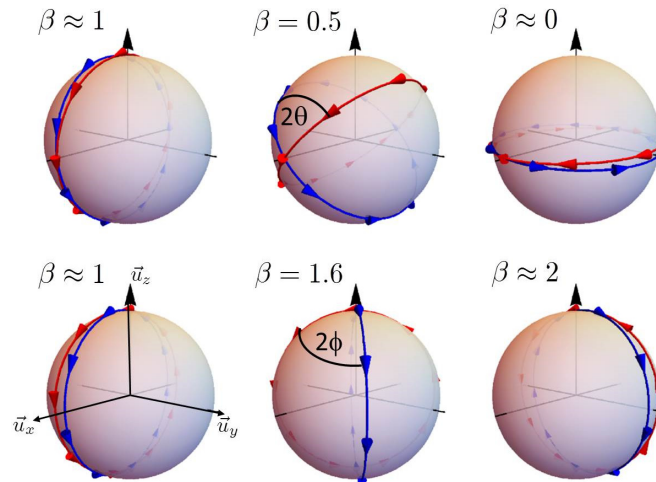


Figure S6. Scheme of the rotation of the winding plane as a function of β for the two Dirac cones (red and blue lines) emerging from the parabolic-flat band touching.

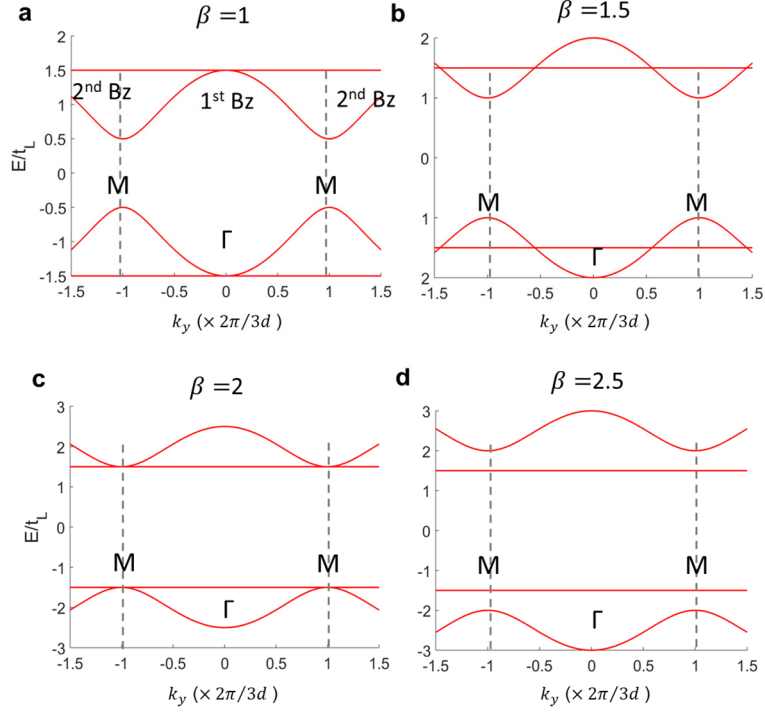


Figure S7. Tight binding spectra for different values of $\beta > 1$ at $k_x = 0$. At $\beta = 2$ the type-III Dirac cones merge and annihilate resulting in a gap opening for $\beta > 2$.

as a function of β . As each of the two emergent Dirac cones is described by an angle θ of opposite sign, the winding plane turns in opposite directions for each Dirac cone when β goes to zero. This is illustrated by the red and blue circles in Fig. S6, which show, respectively, the winding plane of each of the two Dirac cones.

For $\beta > 1$, the vector $\mathbf{h}(\mathbf{q})$ resides on the plane $(\mathbf{u}_\phi, \mathbf{u}_z)$ and the winding vector points in the direction $\frac{\mathbf{w}}{|\mathbf{w}|} = (\pm \sin \phi, \cos \phi, 0)$. Note that at $\beta = 2$ (bottom-right panel in Fig. S6), the two emergent Dirac cones are described by a winding vector residing in the same plane but pointing in opposite directions. Therefore, the winding around each Dirac cone has opposite sign: $\mathcal{W} = +1$ and $\mathcal{W} = -1$. At $\beta = 2$, the Dirac cones merge at the M-point and annihilate, and a gap opens for $\beta > 2$. This situation is shown in Fig. S7, and it could not be observed experimentally because the engineered hoppings in the designed structure were limited to $\beta = 1.5$. This kind of merging preceded by a rotation of the winding plane has been recently discussed in detail in the context of the Mielke lattice under strain⁴.

1. Jacqmin, T. *et al.* Direct Observation of Dirac Cones and a Flatband in a Honeycomb Lattice for Polaritons. *Phys. Rev. Lett.* **112**, 116402 (2014).
2. Wu, C. & Das Sarma, S. p x , y -orbital counterpart of graphene: Cold atoms in the honeycomb optical lattice. *Phys. Rev. B* **77**, 235107 (2008).
3. Cohen-Tannoudji, C., Grynberg, J. & Dupont-Roc, G. *Atom-Photon Interactions: Basic Process and Applications*. (Wiley, 1992).
4. Montambaux, G., Lim, L.-K., Fuchs, J.-N. & Piéchon, F. Winding vector: how to annihilate two Dirac points with the same charge. *arXiv:1804.00781* (2018).